Digest Journal of Nanomaterials and Biostructures Vol. 20, No. 4, October-December 2025, p. 1570-1585

Nitrogen–doped activated carbon from waste biochar for supercapacitor electrode

X. Y. Shen, S. X. Yu, J. H. Mu, J. Li, S. Chen, and F. Xu *
State Key Laboratory of Efficient Production of Forest Resources, Beijing Key Laboratory Lignocellulosic Chemistry, Beijing Forestry University, Beijing, 100083, China

In recent years, biochar has been increasingly used in energy storage devices. Furfural production and formic acid pulping industries offer a large amount of waste biochar, while such carbon-rich feedstocks still remain challenging in value-added utilization. In this study, waste biochar is processed into carbon-based electrodes through activation and nitrogen doping. The as-prepared electrode exhibits a highly porous microtopography and a significantly elevated specific surface area of ~553 $m^2 \cdot g^{-1}$, which provides extensive adsorption sites for charges and promotes the transport of electrolyte ions, thereby delivering a desirable specific capacitance of 464.6 $F \cdot g^{-1}$. The symmetric supercapacitor assembled from such an electrode performs well in long-term cycling experiments, showcasing the coulombic efficiency of 96.3% after conducting 5000 charge/discharge cycles at a given current density (1 $A \cdot g^{-1}$). The utilization of modified waste biochar in electrode materials fabrication not only advances the evolution of sustainable, cost-effective, and high-performance biochar-based energy storage systems but also promotes the value-added utilization of waste biochar.

(Received September 11, 2025; Accepted December 8, 2025)

Keywords: Biochar, Supercapacitors, Carbon-based electrode materials, Activation, Nitrogen doping

1. Introduction

Furfural production and formic acid pulping yield a large amount of solid biochar [1], while it is often discarded as waste or burned as low-grade fuel, thereby limiting its value-added utilization and raising potential environmental risk [2]. Biochar, primarily composed of carbon, hydrogen, oxygen, and ash [3], features abundance, eco-friendliness, low cost, and adsorption properties [4], which have been extensively applied in environmental fields such as pollutant adsorption [5-7] and soil remediation [8-11]. In particular, biochar also exhibits excellent electrical properties, including electrical conductivity and electrochemical stability, thereby performing well in various energy storage systems [12-16]. For example, Zou *et al*. [17] presented the preparation of nitrogen-doped hierarchical porous biochar using biomass-derived bamboo fungus. The resulting porous biochar demonstrated remarkable supercapacitive performance, in particular, achieving a promising specific capacitance of 228 $F \cdot g^{-1}$. Gao *et al*. [18]collected lignocellulose-rich waste inner shells from nuts and converted them into biochar-based materials with a large pore density through carbonization and activation, achieving a specific capacitance of 163 $F \cdot g^{-1}$. These studies collectively demonstrated that the rational design and activation of biochar-based materials could effectively regulate their pore architecture and surface chemistry, thus transforming agricultural and industrial by-products into high-value electrode materials for sustainable energy storage applications.

Supercapacitors, prized by their cycling stability, time-saving charge-discharge capability, and attractive specific capacitance [19], are widely regarded as highly promising devices for energy storage [20, 21]. These energy storage systems are composed of an encapsulated shell, diaphragm, collector, electrolyte, and electrode material [22], among which the electrode material is essential

* Corresponding author: xfx315@bjfu.edu.cn
https://doi.org/10.15251/DJNB.2025.204.1570

for electrochemical performance and practical application [23]. Electrode materials are generally classified into four categories [24]: metal oxides/metal hydroxides [25], conductive polymers [26], composites [27], and carbon-based materials [28]. Carbon-based materials, represented by activated carbon (AC) [29], graphene [30], carbon nanotubes (CNTs) [31], among others, have attracted widespread attention owing to their low density, environmental friendliness, and low resistance. The physical and chemical characterization, such as porosity [32], specific surface area [33], and surface functional groups [34], significantly influence the resulting electrochemical performance of carbon-based electrodes.

Macropores (>50 nm) can store electrolyte ions and facilitate their transport within electrodes, while mesopores (2–50 nm) and micropores (<2 nm) [35] increase the specific surface of electrodes and thus offer more adsorption sites for electrons. These disordered pore structures allow rapid ion diffusion through microporous channels, efficient buffering and charge accumulation in mesopores, and abundant charge adsorption in micropores, thus realizing a synergistic contribution to charge storage. According to the theory of the electric double layer, the specific capacitance of the electrode is positively correlated with its specific surface area [36]. However, an excessively accessible specific surface area may result in a decrease in the mesoporosity, resulting in reduced charge storage capacity. For instance, when micropores dominate, and their diameter is too small to accommodate solvated ions, the diffusion resistance increases significantly, leading to incomplete ion accessibility during the fast charge-discharge process. Therefore, the optimization of the pore structure is significantly crucial for imparting better electrochemical performance to carbon-based electrodes. Physical and/or chemical activation enables the improvement of pore density of carbon-based materials and thus enhances the electrochemical performance of the resulting AC in applications as electrodes for supercapacitors [37, 38]. However, excessive activation may reduce the electrical conductivity together with the contraction of specific surface area for original carbon-based materials, in turn compromising their comprehensive properties in practical applications [39]. For instance, Li *et al*. [40] studied how activation conditions impacted the resulting performance of sargassum-based AC. The research concluded that excessive activation caused the decrease of microporosity and enlarged the mean value of pore size, which in turn reduced the specific surface area and led to the structural failure of pore walls, thereby weakening the electrochemical performance of supercapacitors. In addition, surface functional groups also exert a decisive impact on altering the electrochemical properties of carbon-based materials [41, 42]. The presence of abundant active functional groups enhances the interactions between electrodes and electrolyte, which makes the surface of the obtained electrodes more wettable, thereby contributing to the improvement of their electrical properties [43]. Nitrogen/oxygen-containing groups could improve ion diffusion and interfacial charge transfer by providing additional polar sites, while a moderate amount of such functionalities also strengthens electrolyte wettability and rate capability without compromising conductivity.

In particular, biochar has attracted increasing attention in the development of supercapacitors [44-46]. However, unmodified biochar typically exhibits a disordered structure and low intrinsic activity, thus making it challenging in commercial applications [47]. Its actual specific capacity is only 10%–20% of the theoretical capacity, highlighting the great potential to further improve the properties of biochar by tailoring its porosity and surface functionality through various modification strategies (e.g., activation and hybridization). Activation techniques are generally categorized into chemical, physical, and hybrid methods. When different gases or chemical agents are used at high temperatures, biochar-based materials react to etch and expand the carbon framework, thereby selectively removing disordered carbon atoms and generating the porous network. Heteroatom doping involves introducing non-carbon elements into the carbon framework, which–by substitution or attachment–modifies the electron density, bond lengths, and chemical reactivity of carbon atoms, thus tailoring the electronic structure and chemical properties of biochar-based materials. For example, Burak Tekin's team [48] employed hydrothermal synthesis and KOH activation to process hemp into a carbon-based cathode with a fourfold increase in its surface area, which exhibited a specific capacitance of 220 $F \cdot g^{-1}$, accompanied by remarkable cycling stability (with more than 98% retention of the initial value after 2000 charge/discharge cycles). Syed Comail Abbas *et al*. [49] used bamboo to prepare the SiC/N dual-doped biochar materials. The dual doping promoted the faradaic redox reaction during the charge/discharge cycling process, thereby yielding

an excellent energy density of 5.41 $Wh \cdot kg^{-1}$ when using a power density of 0.5 $kW \cdot kg^{-1}$. In addition, it achieved a specific capacitance of 162 $F \cdot g^{-1}$ in the symmetric supercapacitor.

In this study, waste biochar was processed into a series of carbon-based electrodes based on the collaborative effects of sodium citrate activation and urea nitrogen-doping. As a result, the carbon-based electrodes featured a highly porous architecture, thereby providing them with a superior specific surface area (~553 $m^2 \cdot g^{-1}$) compared with unmodified biochar (~169 $m^2 \cdot g^{-1}$). Additionally, the nitrogen functionality concurrently improved electronic transport and electrolyte wettability, enhancing ion diffusion within the biochar-based electrodes and promoting charge storage at the electrode–electrolyte interface. The assembled symmetric supercapacitor showed excellent long-term cycling stability, which yielded a 96.3% retention of specific capacitance after long-term charge/discharge cycles at a selected current density. Collectively, this work not only delivered carbon-based electrode materials with strong energy storage devices but also contributed to the value-added utilization of solid waste biochar in the hope of supporting the development of sustainable electrochemical energy storage technologies.

2. Experimental

2.1. Materials

Waste biochar was generated during the furfural production and formic acid pulping by Jinan Shengquan Group Co., Ltd. It could be used after washing and drying. Sodium citrate ($Na_3C_6H_5O_7 \cdot 2H_2O$), Carbamide ($CH_4N_2O$), Hydrochloric acid, Sulfuric acid, Ethanol (C_2H_5OH), Potassium bromide, and Polytetrafluoroethylene (PTFE) were purchased from China. The purity level of chemicals was analytical pure. During the whole experiment process, use deionized water.

2.2. Material synthesis

2.2.1. Preparation of RC-X-Y

Waste biochar was completely dried by the baking oven and then ground into a uniform powder for further use. Equal proportions of sodium citrate (as the activating agent) and urea (as the nitrogen source) were added to raw biochar, and all four samples were placed in a tube furnace at 800 °C for 2 h under a nitrogen flow. The cooled products were repeatedly washed with hydrochloric acid and then washed with deionized water until the pH was neutralized.

Samples obtained from the preceding steps were designed as RC (without activating agent or nitrogen source), RC-activated (containing only activating agent), RC-N (containing only nitrogen source), and RC-activated-N (containing both activating agent and nitrogen source).

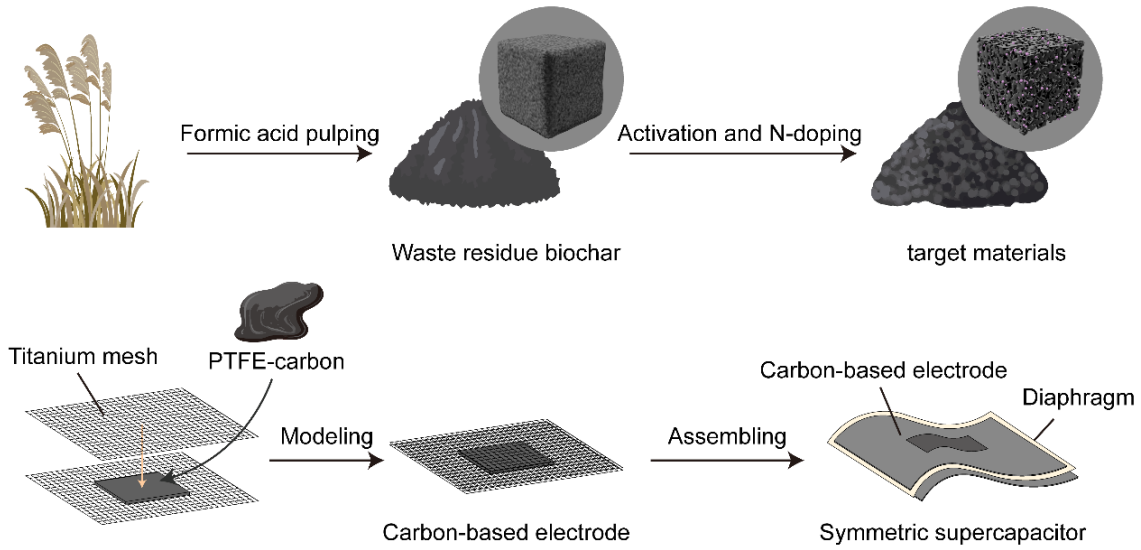

Fig. 1. Schematic of processing waste residue biochar into a symmetric supercapacitor.

2.2.2. Preparation of carbon-based electrodes

A mixture of 95% sample and 5% PTFE was added to ethanol, and the uniform slurry was obtained by using ultrasonication for 30 minutes. To get rid of excess ethanol from the composite material, the mixture was heated in the oven at 12 h. Then, 2 mg of composite material and a piece of nickel foam were used to press square electrodes (10–12 mm in length) under a pressure of 12 MPa. Before testing, the working electrodes needed to be left in the sulfuric acid electrolyte under negative pressure for 30 minutes. Fig. 1 schematically illustrates the experimental sequence.

2.3. Material characterization

The morphology of material surfaces and their characteristic pores were examined using a Scanning Electron Microscope (SEM, S-3400N). Graphitization levels were analyzed by a Raman spectrometer (SENTERRA II). The crystallinity of biochar-based materials was investigated by X-ray diffraction spectroscopy (XRD, X' Pert PRO MPD). Functional group identification for biochar-based materials was determined by a Fourier Transform Infrared Spectrometer (FTIR, TENSOR II). Thermal stability was determined by a Thermal Gravimetric Analyzer (TGA). Specific surface area of biochar-based materials for porosity analysis was conducted by using BET for nitrogen adsorption/desorption isotherm analyses, following the Brunauer-Emmett-Teller method. The elemental composition and atomic percentage of biochar-based materials were assessed by X-ray Photoelectron Spectroscopy (XPS, K-Alpha).

2.4. Electrochemical performance characterization

The electrochemical performance of the obtained electrodes was tested by means of a Metrohm PGSTAT 302F electrochemical workstation. All testing modes, including conventional three-electrode and symmetric two-electrode configurations, had been used. The working electrode for testing was prepared by depositing samples on it. The Pt tablet was used as the counter electrode. Additionally, the saturated calomel electrode (SCE) was used as a reference electrode for testing in conventional three-electrode configurations. All CV, GCD, and EIS analyses had been done in 1 M H_2SO_4 electrolyte. The specific capacitance value (Cm, $F \cdot g^{-1}$) was calculated by analyzing the GCD discharge curve.

At device-level testing, the symmetric supercapacitor was assembled with the RC-activated-N sample used as both electrodes in a two-electrode system. Also, CV, GCD, EIS, and cycling performance tests were conducted in 1 M H_2SO_4 electrolyte.

3. Results and discussion

3.1. Structure characterization

The four biochar-based materials were ground into powders and mounted on a conductive adhesive. Excess powder was removed with the rubber air blower, and the four specimens were sputter-coated with gold to prepare for SEM analysis. SEM images of the four samples (Fig. 2a–d) revealed that the surfaces of RC and RC-N without activation treatment were smooth with dense structure, whereas RC-activated and RC-activated-N exhibited porous and irregular cluster structure [50]. This difference was primarily attributed to the introduction of numerous porous structures into the biochar under the action of the activating agent. At elevated temperature conditions, the activating agent undergoes vigorous chemical reactions with biochar-based materials, releasing various gases such as CO and CO_2, which continuously etch the carbon framework and thereby generate plenty of pores. A comparison between Fig. 2b and Fig. 2d indicated that RC-activated-N possessed a higher pore density than RC-activated, which had not undergone nitrogen doping. The doping of nitrogen accelerated the release of gases and the formation of pores. In addition, partial substitution of carbon atoms in the carbon framework by nitrogen atoms introduced lattice defects and structural strain, contributing to the increment of the pore density and the activity of the porous wall. However, the sole assistance of nitrogen failed to create the desired porous microstructure (Fig.

2c). Instead, nitrogen was more effective in regulating the pore architecture and turning the surface chemical properties. For carbon-based electrodes, the porous structure offers abundant adsorption sites, facilitates charge storage, and promotes the transportation of electrolyte ions, thereby improving the electrochemical performance. Therefore, the combined effects of activation and nitrogen doping not only induced the formation of the pore architecture but also played a critical role in enhancing the functionality of the electrodes.

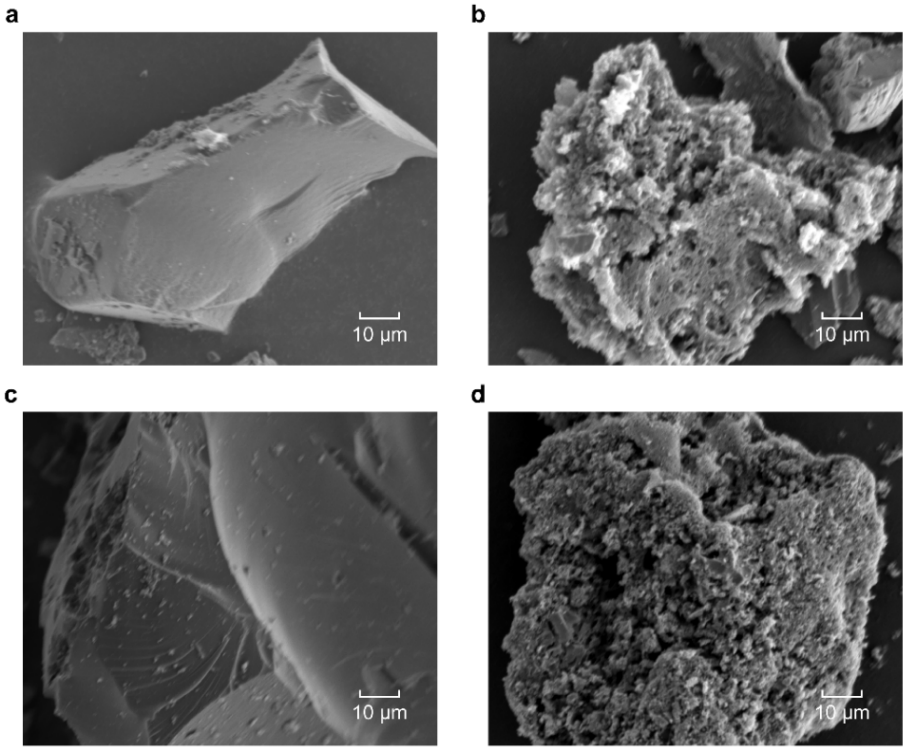

Fig. 2. SEM images of RC (a), RC-activated (b), RC-activated-N (c), and RC-N (d).

According to theory, the D peak (~1350 cm^{-1}) is commonly assigned to defects and disorder in the carbon atomic lattice (sp^3 hybridization), while the G peak (~1580 cm^{-1}) is related to the well-organized structure of graphitized carbon (sp^2 hybridization) [51, 52]. The Raman spectra of four samples (Fig. 3a) displayed two distinct peaks assigned to the D and G bands. It could be observed that RC and RC-N displayed relatively strong intensity of the G peak, indicating a higher degree of graphitization. The I_D/I_G ratios were calculated based on peak intensities (Table 1), and the table effectively captured the processes of carbon structural ordering and defect engineering. A higher ratio demonstrated that more defects in the carbon lattice, as observed in RC-activated and RC-activated-N. These results suggested that both activation and nitrogen doping increased the defects of C atomic crystals, thereby promoting the formation of a porous structure [53].

In the XRD pattern (Fig. 3b), all four samples exhibited diffraction peaks at 24.3° and 43.7°, attributable to the (002) and (100) planes, which reflect the stacking of graphite carbon layers and the in-plane arrangement of carbon atoms [54-56]. These were commonly used indicators for evaluating the degree of graphitization. The sharp diffraction peaks observed in RC and RC-N suggested a relatively high degree of graphitization. In contrast, the diffraction peaks of the other two samples became significantly broader, illustrating a more disordered structure with plenty of micropores. Activation and nitrogen doping disrupted the layered structure of carbon materials, reduced the degree of graphitization, facilitated the formation of a porous structure, and provided more active sites. Such structural changes were consistent with the typical evolution observed in biochar-based materials by activation and nitrogen doping. Also, this result confirmed that the experimental treatment successfully transformed the compact graphite-like structure into a partially

disordered porous structure with accessible active sites, which was highly beneficial for charge storage and electrochemical reaction kinetics in supercapacitors.

Dried biochar-based materials were mixed and ground with KBr at the mass ratio (samples: KBr = 1:100), then pressed into pellets under 8–10 MPa to obtain specimens for FTIR analysis. FTIR spectra displayed that there was a relatively weak absorption peak in the RC at 3200–3600 cm^{-1}, arising mainly from hydroxyl (–OH) stretching (Fig. 3c) [57, 58]. As the strategy of activation and nitrogen doping was executed, the absorption bands of the other three samples became wider. It could indicate that the behavior of activation and nitrogen doping introduced more hydroxy groups in the surface of the materials. The broadened hydroxyl bands also implied an increase in hydrogen-bonding interactions among surface functional groups, which generally contributed to improving wettability and stronger affinity toward electrolyte ions. Similarly, a faint aromatic C=C skeletal vibration around 1600 cm^{-1} in the curve of RC indicates a low abundance of surface polar groups. In addition, RC-N and RC-activated-N emerged peaks at 1540–1570 cm^{-1} and 1200–1350 cm^{-1}, corresponding to N–H bending deformation and C–N stretching vibration, respectively [59]. The coexistence of N–H and C–N bands demonstrated that nitrogen was successfully embedded in biochar-based materials, which could enhance the surface reactivity and electron-donating capability. Infrared spectrum characterization strongly confirmed the formation of porous nitrogen-doped materials.

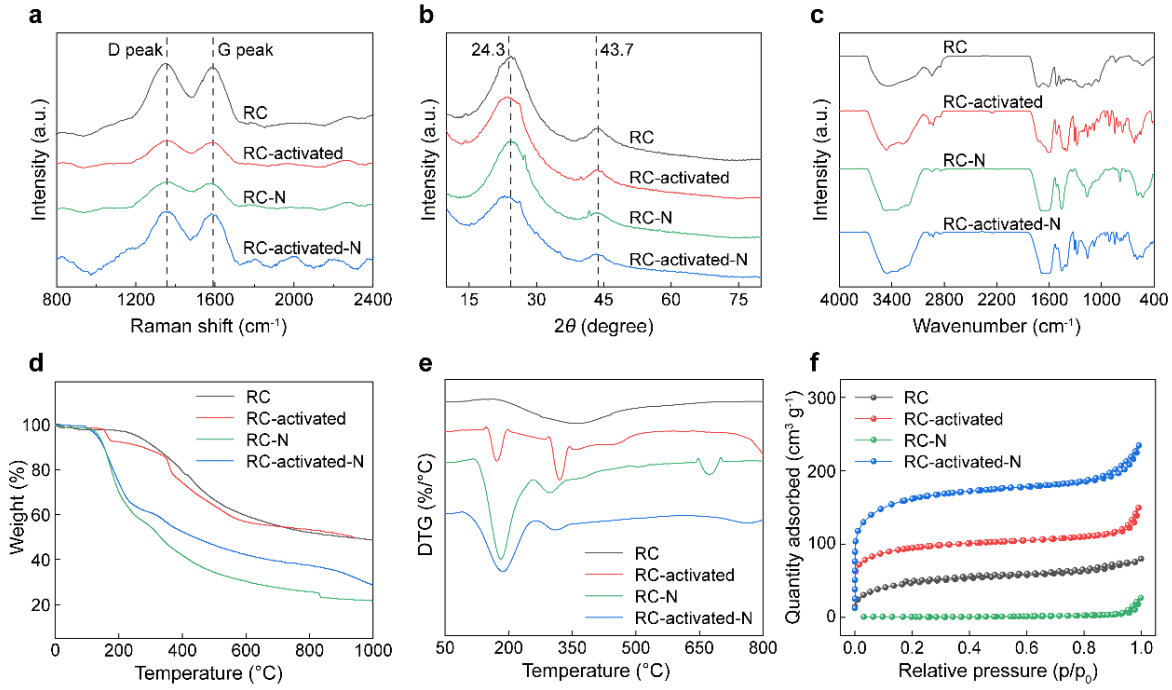

Fig. 3. Raman spectra (a), XRD patterns (b), FTIR spectra (c), TGA profiles (d), DTG profiles (e), and N_2 adsorption-desorption isotherms (f) of the carbon-based electrode materials.

Thermogravimetric analysis (TGA) is a widely used technique for investigating the combustion properties and thermal kinetics of materials. It was generally recognized that the pyrolysis of carbon materials could be segmented into three phases of weight loss. In the initial stage, when the temperature reached approximately 150 °C, moisture and light volatile compounds began to evaporate, with no obvious chemical reaction occurring. This stage mainly corresponded to the removal of physically adsorbed water and a small amount of bound water within the pores, which helped in improving the hydrophilicity and pore accessibility of these materials. With further temperature increase (From 150 to 500 °C), organic functional groups or semi-carbonized components underwent thermal decomposition, and volatile gases were continuously released, resulting in a continuous decrease in mass [54]. At temperatures above 500 °C, the breakdown and recombination of unstable C–C, C–H, and C–O bonds occurred, and the mass loss became less

significant at this stage. These stages were clearly reflected in Fig. 3d. Combined with Fig. 3e, all four samples retained a low carbon residue. This was because the addition of activators and nitrogen-containing agents intensified the consumption of the carbon skeleton, resulting in a relatively small residual carbon content in the end.

Table 1. D peak, G peak, and intensity ratio of the carbon-based electrode materials.

Sample	D peak (%)	G peak (%)	I_D/I_G [a]
RC	59.5034	40.4966	1.4693
RC-activated	60.5169	39.4831	1.5327
RC-N	65.0425	34.9575	1.4471
RC-activated-N	68.9781	31.0219	2.2235

[a] I_D/I_G values were calculated by the area ratio of D peak to G peak.

According to the significant differences in the N_2 adsorption-desorption isotherms (Fig. 3f), it was clear that the microstructure of four carbon-based materials exhibited distinctive characteristics. It could be observed that RC exhibited a slight increase in adsorption at low relative pressures, while RC-N had no significant increase, indicating the absence of abundant micropores in both. In contrast, the adsorption amount of RC-activated rose rapidly at low relative pressures and subsequently reached a saturated state at relatively higher pressures. This result is considered a typical characteristic of the Type I isotherm, which suggests the presence of numerous micropores within the microstructure of RC-activated. Notably, the adsorption curve of RC-activated-N showed a hysteresis loop at a relative pressure of about 0.8, indicative of the Type IV isotherm [60]. The emergence of such a curve was a typical signature of capillary condensation within mesoporous regions, suggesting that nitrogen doping promoted the development of a disordered porous structure. Moreover, its overall adsorption was higher than that of RC-activated, indicating the coexistence of both abundant micropores and a certain amount of mesopores. By calculating the BET curves, RC-activated-N exhibited a specific surface area of ~553 $m^2 \cdot g^{-1}$, significantly outperforming those of RC (~169 $m^2 \cdot g^{-1}$), RC-activated (~312 $m^2 \cdot g^{-1}$), and RC-N (~2 $m^2 \cdot g^{-1}$). Comparative analysis revealed that activation and nitrogen doping increased more microporous structures and improved the adsorption capacity, contributing to the larger electrochemical active interfacial area. These findings were consistent with the characterization of the samples in the SEM, Raman, and XRD.

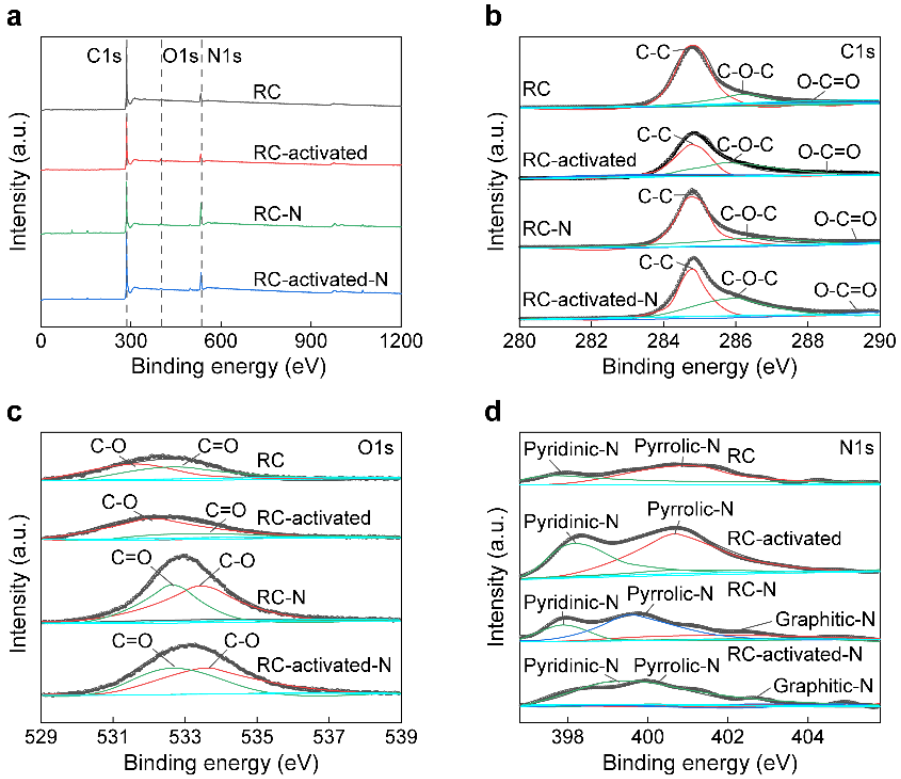

Fig. 4. Total XPS spectrum (a), C1s (b), O1s (c), and N1s spectra (d) of the carbon-based electrode materials.

Table 2 Composition of the carbon-based electrode materials.

Sample	C (%)	O (%)	N (%)
RC	76.33	16.26	1.58
RC-activated	66.24	25.37	2.69
RC-N	60.01	30.73	3.13
RC-activated-N	63.93	32.74	3.33

The XPS survey spectra (Fig. 4a) showed characteristic peaks corresponding to C1s (~285 eV), O1s (~533 eV), and N1s (~400 eV). From these spectra, along with information in Table 2, it was clear that both RC-activated-N and RC-N showed nearly twice the amount of N element compared to RC and RC-activated, which confirmed that nitrogen was present in the biochar itself and that successful doping had been done. Precision high-resolution spectra for elements were taken for better identification of variations in functional groups for samples. The high-resolution C1s spectra could be separated for all samples with three peaks for 284.8, 285.9 and 289.1 eV, corresponding to elements with a binding energy for C–C, C–O–C, and O–C=O (Fig. 4b). Similarly, high-resolution spectra for O1s could be separated with two peaks for 532.6 and 532.9 eV, corresponding to elements with binding energy for C–O and C=O (Fig. 4c) [61, 62]. Also, it was interesting to note that peaks corresponding to oxygen-containing functional groups for samples after activation had been intensified, signifying that oxygen-containing functional groups were introduced by chemical activation. As we know, oxygen-containing functional groups have been found to play a pivotal role in charge storage capacity for biochar-based electrode materials. A higher concentration of the C=O group increased the hydrophilicity of the carbon materials and contributed to pseudocapacitance, resulting in excellent site-specific catalytic properties and charge transfer efficiency during cycling. In the N1s spectra (Fig. 4d), all four samples showed two peaks of pyridinic-N and pyrrolic-N, indicating that nitrogen atoms had substituted for a portion of carbon atoms in the carbon framework. Pyridinic-N, located at edges or vacancies, readily interacted with

oxygen atom, hydrogen atom, or electrolyte ions, thereby promoting pore-wall activation and ion adsorption. It also provided active sites for electron-conduction pathways and reaction centers. Pyrrolic-N could contribute pseudocapacitance and catalytic activity, improve the wettability and interfacial compatibility between biochar-based materials and the electrolyte, and might transform into graphitic-N at high temperature, thus optimizing the carbon framework. Graphitic-N was additionally observed in the nitrogen-doped samples. The ratio of graphitic-N in RC-activated-N was higher than in RC-N, and the emergence of graphitic-N helped to enhance electronic conductivity, which was more beneficial to the performance of supercapacitors (including energy storage, electrocatalysis, and ion adsorption).

3.2. Electrochemical performance characterization

Electrochemical measurements of carbon-based electrodes were conducted in 1M H_2SO_4 solution electrolyte with the standard three-electrode setup (Fig. 5). As shown in Fig. 5a, the CV traces of the four electrodes were recorded at a scanning rate of 100 $mV \cdot s^{-1}$. Among them, RC-activated-N exhibited the largest enclosed area, consistent with a substantially enlarged electrochemically accessible surface generated by activation and nitrogen doping, together with plentiful active sites. Both RC-activated and RC-activated-N displayed nearly rectangular CV profiles, characteristic of efficient charge transfer and dominant electrical double-layer capacitance (EDLC) behavior [63]. The overall CV curves remained largely preserved across a range of scanning rates (Fig. S1), supporting the robustness of the capacitive response. In addition, the samples with activation exhibited slight distortion, which could be attributed to pseudocapacitance arising from oxygen/nitrogen-containing functional groups. A more detailed electrochemical evaluation of four samples (Fig. 5b–c and Fig. S2) revealed that RC-activated-N maintained well-defined curve shapes without drastic shape deformation across different scanning rates, suggesting excellent rate capability and electrochemical performance.

Fig. 5d shows the GCD curves of the four carbon-based materials, recorded at a current density of 1 $A \cdot g^{-1}$. The discharge duration directly reflected the specific capacitance of the electrode, with RC-activated-N demonstrating the longest discharge time, and thus the highest specific capacity of 311.2 $F \cdot g^{-1}$ at the current density of 1 $A \cdot g^{-1}$. This trend was also observed at other current densities (Fig. S3). Among them, RC-activated-N exhibited a specific capacitance of 464.6 $F \cdot g^{-1}$ at 0.1 $A \cdot g^{-1}$, which is markedly higher than those of RC (79.8 $F \cdot g^{-1}$), RC-activated (133.4 $F \cdot g^{-1}$), and RC-N (64.8 $F \cdot g^{-1}$). Combining the GCD curves of four samples (Fig. 5e–f and Fig. S4), it was evident that RC and RC-N exhibited much shorter charge-discharge time than RC-activated and RC-activated-N, indicating substantially reduced capacitance [64]. Notably, the GCD curves of RC-activated-N (Fig. 5f) maintained a nearly symmetric isosceles triangular shape, even though the current densities were further increased. This indicated a highly reversible charge-discharge process dominated by EDLC. The electrode prepared by RC-activated-N exhibited excellent electrical conductivity, low internal resistance, and facile ion transport, reflecting outstanding electrochemical stability and energy efficiency. However, the other samples displayed distorted, irregular shapes with rapidly shortened discharge time. These results confirmed that the porous structure of RC-activated-N facilitated rapid electron transport and ensured good cycling reversibility.

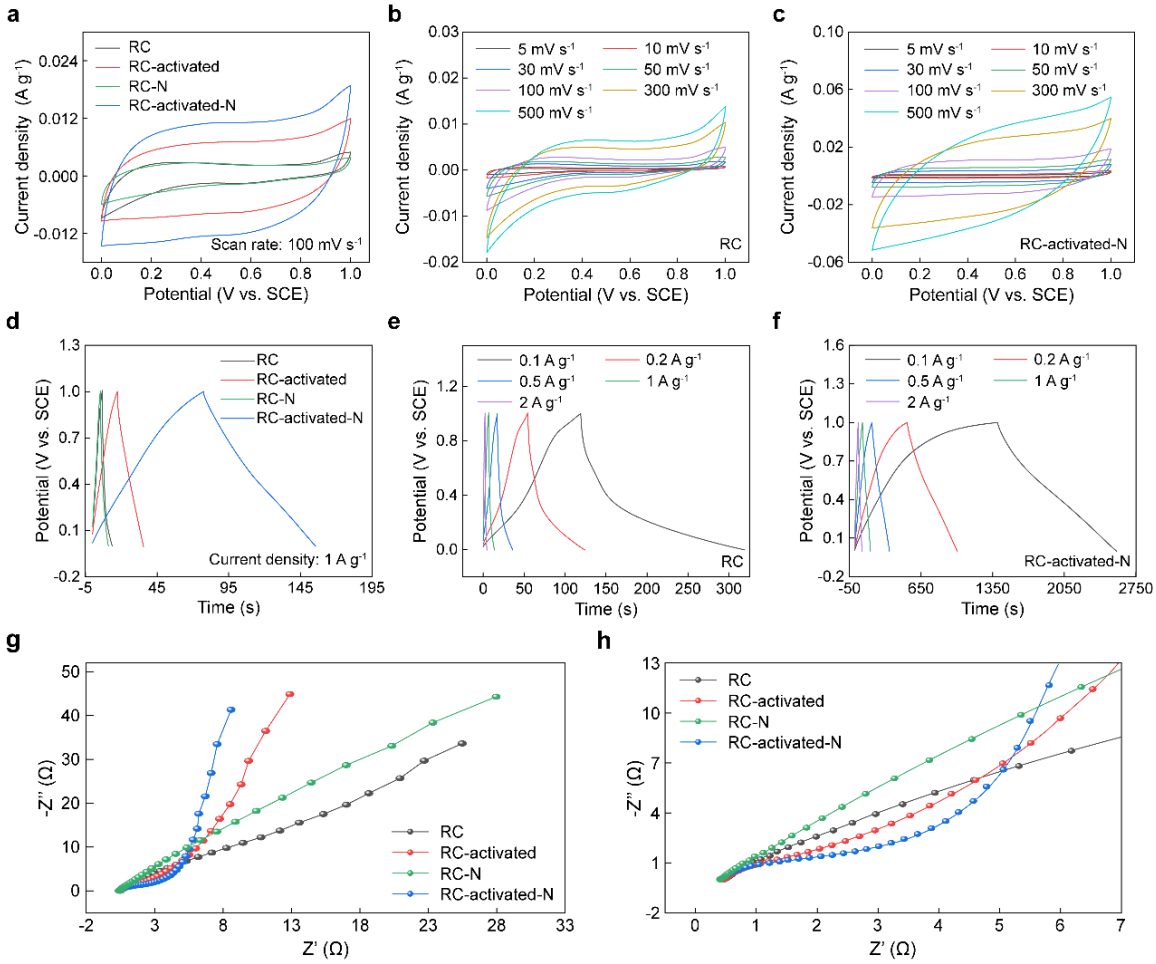

Fig. 5. *Electrochemical performance in 1M H_2SO_4 electrolyte with the three-electrode system: (a) CV curves of the carbon-based electrode materials were obtained at the scanning rate of 100 mV·s^{-1}, (b) RC, and (c) RC-activated-N at different scanning rates. (d) GCD curves of four samples were obtained at the current density of 1 A·g^{-1}, (e) RC and (f) RC-activated-N at different current densities. (g) Nyquist plots with fitting profiles and (h) enlarged high-frequency regions of four samples.*

Fig. 5g–h presented the Nyquist plots with fitting profiles and enlarged high-frequency regions for four samples. In general, the high-frequency segment of the Nyquist diagram exhibited a quasi-semicircle, corresponding to the interfacial charge transfer process under kinetic control, whereas the low-frequency segment approached a straight line, associated with ion diffusion under mass transport control [65]. In the high-frequency segment, the semicircular arc radius reflects the charge-transfer resistance, whereas a steeper low-frequency segment slope denotes better characteristics of EDLC and higher capacitance. Among the four samples, RC-activated-N exhibited the smallest intercept and the minimal semi-circular diameter in the high-frequency segment, as well as the steepest slope in the low-frequency segment. These features indicated that RC-activated N possessed low resistance, facilitated faster and more reversible charge transfer both at the surface and across the interior for the majority of the electrodes, and approached ideal capacitive behavior with minimal ion diffusion resistance.

Taken together, the structural characterizations and electrochemical results suggested that the superior electrochemical performance of RC-activated-N arose from its high density of electrochemically addressable sites for charge storage, combined with a multiscale porous structure that greatly enhanced specific surface area and accessibility. This architecture promoted efficient electrolyte ion transport, thereby enhancing their overall electrochemical energy storage behavior of the electrodes.

To investigate the actual electrochemical performance of RC-activated-N, a symmetric supercapacitor was fabricated and characterized in 1 M H_2SO_4 electrolyte. The CV test showed that all CV profiles demonstrated a rectangle-like profile without any obvious deviation even with high scanning rates (Fig. 6a). This result clearly confirmed that this supercapacitor demonstrated a normal double-layer capacitance performance with excellent rate capability. From the GCD profiles in Fig. 6b, it could be found that all profiles showed a rough isosceles triangle. This result clearly confirmed that this supercapacitor demonstrated robust capacitance performance and low resistance for assembled electrode. In Fig. 6c, the high-frequency segment of Nyquist plots with curves represents low internal resistance of electrode. Meanwhile, the curves in low-frequency segment approached vertical, suggesting that the ion diffusion process on the electrode surface was close to the ideal capacitive behavior. Collectively, three results demonstrated that the assembled supercapacitor possessed excellent capacitive behaviors, comparable to or even exceeding those of many previously reported biochar-based electrode materials.

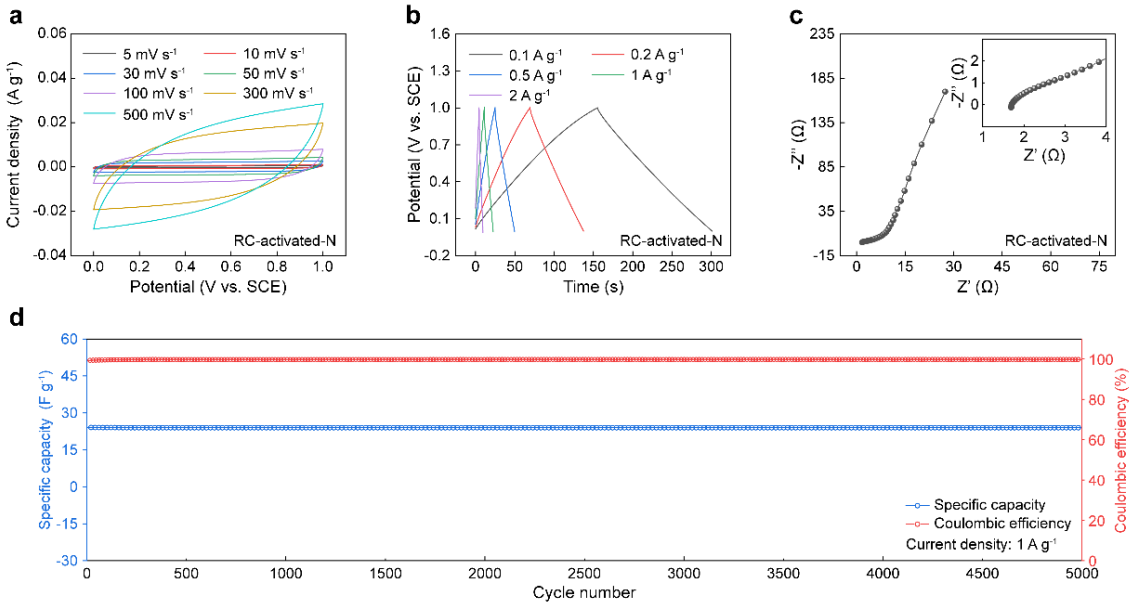

Fig. 6. Electrochemical performance of RC-activated-N in the two-electrode system. (a) CV curves at different scanning rates from 5 to 500 mV·s^{-1}, (b) GCD curves at different current densities from 0.1 to 2 A·g^{-1}, (c) Nyquist plots with fitting profiles and enlarged high frequency region, and (d) specific capacity and coulombic efficiency at a current density of 1 A·g^{-1} after 5000 charge/discharge cycles.

Cycling durability was another significant parameter of supercapacitors. Accordingly, cycling performance was tested under all current densities. According to the formula for calculation, it could be found that RC-activated-N maintained around 28.4 F·g^{-1} for specific capacitance with a current density of 0.2 A·g^{-1}. However, with a gradual increase in current densities ranging from 0.5 to 1 A·g^{-1}, the diffusion rate for electrolyte ions in micro/mesopores began to affect samples, ultimately decreasing their accessible area and reactive sites on the electrodes. These reasons caused a characteristic decline in specific capacitance (from 25.0 to 24.0 F·g^{-1}) with increasing current densities. For instance, at 1 A·g^{-1} current density (Fig. 6d), it was found that there was no decay in specific capacitance, and the coulombic efficiency was about 96.3% for 5000 cycles [66]. Similar trends were observed in the tests conducted at 0.2 and 0.5 A·g^{-1} current densities (Fig. S5). These experimental outcomes revealed that RC-activated-N samples had a stable structure without surface chemical degradation and maintained good electrochemical performance.

4. Conclusions

In this study, the high-performance carbon-based electrode material (RC-activated-N) was successfully prepared by activation and nitrogen doping. The results showed that activation significantly enhanced micropore formation of RC-activated-N, while nitrogen doping improved its electrical conductivity. The cooperative impact of both activation and nitrogen doping endowed RC-activated-N with a highly porous architecture, thereby yielding a markedly increased specific surface area (~553 $m^2 \cdot g^{-1}$). Such porous microstructure exhibited its advantages in providing numerous electrochemically active sites, which significantly facilitated both ion diffusion and charge transport. Consistent with these structural advantages, RC-activated-N exhibited a large specific capacitance of 464.6 $F \cdot g^{-1}$ at the current density of 0.1 $A \cdot g^{-1}$, along with desirable rate capability and excellent cycling stability—surpassing the comparison electrodes (RC, RC-activated, and RC-N). Benefiting from its porosity and plentiful surface functional groups, RC-activated-N exhibited improved ion transport and lowered charge-transfer resistance, resulting in excellent EDLC. Furthermore, the capacitor exhibited stable cycling with negligible decay and a coulombic efficiency of 96.3% after 5000 cycles in the symmetric supercapacitor setup. This study affords a straightforward, scalable strategy for fabricating high-performance carbon-based electrode materials. Meanwhile, the approach couples advanced devices for storing energy with meaningful resource upcycling, enabling the valorization of biochar derived from waste residues.

Availability of Data and Materials

The datasets used and analyzed during the current study are available from the corresponding author on reasonable request.

Author Contributions

F.X. and S.C. conceived the concept and supervised the work. X.S. and S.Y. drew the schematics and graphs. F.X., S.C., J.M., and X.S. contributed to document arrangement and manuscript structure. F.X., S.C., J.M., J.L., and X.S. discussed the design of pictures. X.S. wrote the manuscript, S.C., S.Y., J.L., and X.S. revised the manuscript. All authors commented on the submitted version of the manuscript.

Acknowledgements

This work is supported by the National Natural Science Foundation of China (No. U22A20422), Beijing Nova Programme Interdisciplinary Cooperation Project (20240484611), and 5·5 Engineering Research & Innovation Team Project of Beijing Forestry University (No. BLRC2023B01).

Funding

This project was supported by the National Natural Science Foundation of China (No. U22A20422), Beijing Nova Programme Interdisciplinary Cooperation Project (20240484611), and 5·5 Engineering Research & Innovation Team Project of Beijing Forestry University (No. BLRC2023B01).

Conflict of Interest

The authors declare no conflict of interest.

Appendix A. Supplementary data

Supplementary data to this article can be found online at

References

[1] G. Machado, S. Leon, F. Santos, R. Lourega, J. Dullius, M. E. Mollmann, P. Eichler, Natural Resources **7**(3), 115-127 (2016). https://doi.org/10.4236/nr.2016.73012

[2] M. Lee, Y. Lin, P. T. Chiueh, W. Den, Journal of Cleaner Production **251**, 119714 (2020). https://doi.org/10.1016/j.jclepro.2019.119714

[3] W. Buss, O. Mašek, M. Graham, D. Wüst, Journal of Environmental Management **156**, 150-158 (2015). https://doi.org/10.1016/j.jenvman.2015.03.035

[4] J. S. Cha, S. H. Park, S.-C. Jung, C. Ryu, J.-K. Jeon, M.-C. Shin, Y.-K. Park, Journal of Industrial and Engineering Chemistry **40**, 1-23 (2016). https://doi.org/10.1016/j.jiec.2016.06.002

[5] Z. Fu, J. Zhao, D. Guan, Y. Wang, J. Xie, H. Zhang, Y. Sun, J. Zhu, L. Guo, Science of The Total Environment **912**, 168822 (2024). https://doi.org/10.1016/j.scitotenv.2023.168822

[6] T. U. Vandana, B. K. Tripathy, R. K. Mishra, A. Sharma, K. Mohanty, Process Safety and Environmental Protection **201**, 107505 (2025). https://doi.org/10.1016/j.psep.2025.107505

[7] Y. Liu, Y. Xin, Z. Sun, J. Wan, Z. Li, Z. Shang, X. Zhang, W. Li, J. Luan, Carbon **238**, 120200 (2025). https://doi.org/10.1016/j.carbon.2025.120200

[8] A. Fakhar, R. C. Canatoy, S. J. C. Galgo, M. Rafique, R. Sarfraz, Fuel **400**, 135745 (2025). https://doi.org/10.1016/j.fuel.2025.135745

[9] L. He, Y. Wang, R. Liu, Y. Wang, Y. Wang, Y. Li, F. Zhou, Y. Qiu, Y. Liu, X. Luo, J. Gong, H. Zheng, F. Li, Chemical Engineering Journal Advances **22**, 100758 (2025). https://doi.org/10.1016/j.ceja.2025.100758

[10] Y. Li, Y. Guan, L. Zhang, Chemical Engineering Journal **520**, 166340 (2025). https://doi.org/10.1016/j.cej.2025.166340

[11] X. Yuan, S. Li, F. Yang, S. Wang, S. Bie, Z. Wang, H. Zhang, J. Liu, J. Zhou, X. Wang, D. Liu, C. Feng, Ecotoxicology and Environmental Safety **292**, 117927 (2025). https://doi.org/10.1016/j.ecoenv.2025.117927

[12] S. Rawat, T. Boobalan, B. B. Krishna, M. Sathish, S. Hotha, T. Bhaskar, Chemistry – An Asian Journal **17**(24), e202200982 (2022). https://doi.org/10.1002/asia.202200982

[13] F. Mahmood, M. Ali, M. Khan, C. F. M. Mbeugang, Y. M. Isa, A. Kozlov, M. Penzik, X. Xie, H. Yang, S. Zhang, B. Li, Industrial Crops and Products **227**, 120830 (2025). https://doi.org/10.1016/j.indcrop.2025.120830

[14] A. I. J, C. G, M. M. L, R. S, K. C, N. K. Saravanakumar, M. G, J. Jayaprakash, K. Nagarasampatti Palani, Future Batteries **6**, 100077 (2025). https://doi.org/10.1016/j.fub.2025.100077

[15] Z. Zhao, L. Sun, Y. Li, W. Feng, Carbon **210**, 118066 (2023). https://doi.org/10.1016/j.carbon.2023.118066

[16] B. Jaleh, M. Nasrollahzadeh, M. Eslamipanah, A. Nasri, E. Shabanlou, N. R. Manwar, R. Zboril, P. Fornasiero, M. B. Gawande, Carbon **198**, 301-352 (2022). https://doi.org/10.1016/j.carbon.2022.07.023

[17] Z. Zou, Y. Lei, Y. Li, Y. Zhang, W. Xiao, Molecules **24**(20), 3677 (2019). https://doi.org/10.3390/molecules24203677

[18] M. Gao, W.-K. Wang, Y.-M. Zheng, Q.-B. Zhao, H.-Q. Yu, Chemical Engineering Journal **402**, 126171 (2020). https://doi.org/10.1016/j.cej.2020.126171

[19] N. Kumar, S. B. Kim, S. Y. Lee, S. J. Park, Nanomaterials **12**(20), 3708 (2022). https://doi.org/10.3390/nano12203708

[20] J. Sun, B. Luo, H. Li, Advanced Energy and Sustainability Research **3**(6), 2100191 (2022). https://doi.org/10.1002/aesr.202100191

[21] S. Sharma, P. Chand, Results in Chemistry **5**, 100885 (2023). https://doi.org/10.1016/j.rechem.2023.100885

[22] Yaseen, M. Khattak, M. Humayun, M. Usman, S. S. Shah, S. Bibi, S. U. H. Bakhtiar, S. Ahmad, A. Khan, N. Shah, A. Tahir, H. Ullah, Energies **14**(23), 7779 (2021). https://doi.org/10.3390/en14227779

[23] Y. Zhang, H. Feng, X. Wu, L. Wang, A. Zhang, T. Xia, H. Dong, X. Li, L. Zhang, International Journal of Hydrogen Energy **34**(11), 4889-4898 (2009). https://doi.org/10.1016/j.ijhydene.2009.04.005

[24] Reenu, Sonia, L. Phor, A. Kumar, S. Chahal, Journal of Energy Storage **84**, 110698 (2024). https://doi.org/10.1016/j.est.2024.110698

[25] P. Pazhamalai, V. Krishnan, M. S. Mohamed Saleem, S.-J. Kim, H.-W. Seo, Nano Convergence **11**(1), 30 (2024). https://doi.org/10.1186/s40580-024-00437-2

[26] Q. Meng, K. Cai, Y. Chen, L. Chen, Nano Energy **36**, 268-285 (2017). https://doi.org/10.1016/j.nanoen.2017.04.040

[27] D. E. Tallman, S. L. Petersen, Electroanalysis **2**(7), 499-506 (1990). https://doi.org/10.1002/elan.1140020702

[28] Q. Zhou, H. Yao, Energy Reports **8**, 656-664 (2022). https://doi.org/10.1016/j.egyr.2022.09.167

[29] M. A. Yahya, M. H. Mansor, W. A. A. W. Zolkarnaini, N. S. Rusli, A. Aminuddin, K. Mohamad, F. A. M. Sabhan, A. A. A. Atik, L. N. Ozair, AIP Conference Proceedings **1972**(1), 030028 (2018). https://doi.org/10.1063/1.5041244

[30] J. Ran, Y. Liu, H. Feng, H. Shi, Q. Ma, Journal of Industrial and Engineering Chemistry **137**, 106-117 (2024). https://doi.org/10.1016/j.jiec.2024.03.043

[31] H. Meskher, D. Ghernaout, A. K. Thakur, F. S. Jazi, Q. F. Alsalhy, S. S. Christopher, R. Sathyamurthy, R. Saidur, Materials Today Communications **38**, 108517 (2024). https://doi.org/10.1016/j.mtcomm.2024.108517

[32] F. Lufrano, P. Staiti, International Journal of Electrochemical Science **5**(6), 903-911 (2010). https://doi.org/10.1016/S1452-3981(23)15331-4

[33] H. Li, Y. Ma, Y. Wang, C. Li, Q. Bai, Y. Shen, H. Uyama, Renewable Energy **224**, 120144 (2024). https://doi.org/10.1016/j.renene.2024.120144

[34] X. He, W. Li, Y. Xia, H. Huang, X. Xia, Y. Gan, J. Zhang, W. Zhang, Carbon **210**, 118090 (2023). https://doi.org/10.1016/j.carbon.2023.118090

[35] H. Li, Y. Ma, X. Zhang, X. Zhang, L. Di, Materials **17**(14), 3529 (2024). https://doi.org/10.3390/ma17143529

[36] E. Taer, A. Agus, R. Farma, R. Taslim, A. Awitdrus, M. Paiszal, A. Ira, S. Dini Yardi, Y. Sari, H. Yusra, S. Nurjanah, S. Hartati, Z. Aini, R. Setiadi, Journal of Physics: Conference Series **1116**(3), 032040 (2018). https://doi.org/10.1088/1742-6596/1116/3/032040

[37] M. Pulikkottil, P. Joy, M. M. N, V. Gopalan, A. Seema, Chemical Engineering & Technology **44**(5), 844-852 (2021). https://doi.org/10.1002/ceat.202000450

[38] L. Xie, F. Su, L. Xie, X. Guo, Z. Wang, Q. Kong, G. Sun, A. Ahmad, X. Li, Z. Yi, C. Chen, Materials Chemistry Frontiers **4**(9), 2610-2620 (2020). https://doi.org/10.1039/D0QM00180E

[39] A. M. Abioye, F. N. Ani, Renewable and Sustainable Energy Reviews **52**, 1282-1293 (2015). https://doi.org/10.1016/j.rser.2015.07.129

[40] S. Li, X. Tan, H. Li, Y. Gao, Q. Wang, G. Li, M. Guo, Scientific Reports **12**(1), 10106 (2022). https://doi.org/10.1038/s41598-022-14214-w

[41] H. Cao, X. Peng, M. Zhao, P. Liu, B. Xu, J. Guo, RSC Advances **8**(6), 2858-2866 (2018). https://doi.org/10.1039/C7RA12425B

[42] L. S. Oliveira, J. F. G. Alba, V. L. Silva, R. T. Ribeiro, E. H. L. Falcão, M. Navarro, Journal of Electroanalytical Chemistry **818**, 106-114 (2018). https://doi.org/10.1016/j.jelechem.2018.04.022

[43] N. P. Wickramaratne, J. Xu, M. Wang, L. Zhu, L. Dai, M. Jaroniec, Chemistry of Materials **26**(9), 2820-2828 (2014). https://doi.org/10.1021/cm5001895

[44] C. Pan, Y. Ji, S. Ren, T. Lei, L. Dong, Molecules **30**(1), 89 (2025). https://doi.org/10.3390/molecules30010089

[45] S. Koutcheiko, V. Vorontsov, Journal of Biobased Materials and Bioenergy **7**(6), 733-739 (2013). https://doi.org/10.1166/jbmb.2013.1375

[46] L. Lu, Y. Lan, Q. Zhang, J. Deng, L. Luo, Q. Zeng, H. Gao, Z. Weigang, Journal of Energy Storage **55**, 105839 (2022). https://doi.org/10.1016/j.est.2022.105839

[47] Z. Zeng, L. Yan, G. Li, P. Rao, Y. Sun, Z. Zhao, Carbon **216**, 118543 (2024). https://doi.org/10.1016/j.carbon.2023.118543

[48] B. Tekin, Y. Topcu, Journal of Energy Storage **77**, 109879 (2024). https://doi.org/10.1016/j.est.2023.109879

[49] S. C. Abbas, C. Lin, Z. Hua, Q. Deng, H. Huang, Y. Ni, S. Cao, X. Ma, Chemical Engineering Journal **433**, 133738 (2022). https://doi.org/10.1016/j.cej.2021.133738

[50] H. Lyu, Z. Yu, B. Gao, F. He, J. Huang, J. Tang, B. Shen, Environmental Science and Pollution Research **26**(14), 14693-14704 (2019). https://doi.org/10.1007/s11356-019-04899-4

[51] J. Jiang, L. Zhang, X. Wang, N. Holm, K. Rajagopalan, F. Chen, S. Ma, Electrochimica Acta **113**, 481-489 (2013). https://doi.org/10.1016/j.electacta.2013.09.121

[52] Y. Wang, D. C. Alsmeyer, R. L. Mccreery, Chemistry of Materials **2**(5), 557-563 (1990). https://doi.org/10.1021/cm00011a018

[53] D. B. Schuepfer, F. Badaczewski, J. M. Guerra-Castro, D. M. Hofmann, C. Heiliger, B. Smarsly, P. J. Klar, Carbon **161**, 359-372 (2020). https://doi.org/10.1016/j.carbon.2019.12.094

[54] J.-R. Wang, F. Wan, Q.-F. Lü, F. Chen, Q. Lin, Journal of Materials Science & Technology **34**(10), 1959-1966 (2018). https://doi.org/10.1016/j.jmst.2018.01.005

[55] Z.-W. Ma, H.-Q. Liu, Q.-F. Lü, Journal of Energy Storage **40**, 102773 (2021). https://doi.org/10.1016/j.est.2021.102773

[56] D.-J. Ryu, R.-G. Oh, Y.-D. Seo, S.-Y. Oh, K.-S. Ryu, Environmental Science and Pollution Research **22**(14), 10405-10414 (2015). https://doi.org/10.1007/s11356-015-4348-3

[57] T. Liu, X. Guo, W. Liu, C. Hao, L. Wang, W. C. Hiscox, C. Liu, C. Jin, J. Xin, J. Zhang, Green Chemistry **19**(18), 4364-4372 (2017). https://doi.org/10.1039/C7GC01737E

[58] Ö. Özgenç, S. Durmaz, BioResources **12**(4), 9143-9151 (2017). https://doi.org/10.15376/biores.12.4.9143-9151

[59] G. Hristea, M. Iordoc, E.-M. Lungulescu, I. Bejenari, I. Volf, Scientific Reports **14**(1), 1095 (2024). https://doi.org/10.1038/s41598-024-51350-x

[60] D. V. Cuong, P.-C. Wu, N.-L. Liu, C.-H. Hou, Separation and Purification Technology **242**, 116813 (2020). https://doi.org/10.1016/j.seppur.2020.116813

[61] Y. Tan, W. Dong, Y. Li, R. Muchakayala, L. Kong, L. Kang, F. Ran, New Journal of Chemistry **42**(22), 17895-17904 (2018). https://doi.org/10.1039/C8NJ02404A

[62] C. Wan, J. Li, RSC Advances **6**(89), 86006-86013 (2016). https://doi.org/10.1039/C6RA17044G

[63] J. Liu, J. Essner, J. Li, Chemistry of Materials **22**(17), 5022-5030 (2010). https://doi.org/10.1021/cm101591p

[64] W. Hu, F. Xie, Y. Li, Z. Wu, K. Tian, M. Wang, L. Pan, L. Li, Langmuir **33**(46), 13364-13372 (2017). https://doi.org/10.1021/acs.langmuir.7b03175

[65] Y. Ding, T. Wang, D. Dong, Y. Zhang, Frontiers in Energy Research **7**, 159 (2019). https://doi.org/10.3389/fenrg.2019.00159

[66] G. Byatarayappa, V. Guna, K. Venkatesh, N. Reddy, N. Nagaraju, K. Nagaraju, Journal of Environmental Chemical Engineering **9**(6), 106525 (2021). https://doi.org/10.1016/j.jece.2021.106525